

Dynamics of Rotating Accretion Flows Irradiated by a Quasar

Daniel Proga¹, Jeremiah P. Ostriker², and Ryuichi Kurosawa¹

ABSTRACT

We study the axisymmetric, time-dependent hydrodynamics of rotating flows that are under the influence of supermassive black hole gravity and radiation from an accretion disk surrounding the black hole. This work is an extension of the earlier work presented by Proga, where nonrotating flows were studied. Here, we consider effects of rotation, a position-dependent radiation temperature, density at large radii, and uniform X-ray background radiation. As in the non-rotating case, the rotating flow settles into a configuration with two components (1) an equatorial inflow and (2) a bipolar inflow/outflow with the outflow leaving the system along the pole. However, with rotation the flow does not always reach a steady state. In addition, rotation reduces the outflow collimation and the outward flux of mass and kinetic energy. Moreover rotation increases the outward flux of the thermal energy and can lead to fragmentation and time-variability of the outflow. We also show that a position-dependent radiation temperature can significantly change the flow solution. In particular, the inflow in the equatorial region can be replaced by a thermally driven outflow. Generally, as it have been discussed and shown in the past, we find that self-consistently determined preheating/cooling from the quasar radiation can significantly reduce the rate at which the central BH is fed with matter. However, our results emphasize also a little appreciated feature. Namely, quasar radiation drives a non-spherical, multi-temperature and very dynamic flow. These effects become dominant for luminosities in excess of 0.01 of the Eddington luminosity.

Subject headings: accretion, accretion disks – galaxies: active – galaxies: nuclei – methods: numerical – quasars: general

¹Department of Physics, University of Nevada, Las Vegas, NV 89154, USA: dproga@physics.unlv.edu, rk@physics.unlv.edu

²Princeton University Observatory, Princeton, USA: ostriker@astro.princeton.edu

1. Introduction

The key property of Active Galactic Nuclei (AGN) is that they emit enormous amount of electromagnetic radiation over a very broad energy range. The AGN central location in their host galaxies imply that AGN radiation can play a very important role in determining the ionization structure and dynamics of matter not only near the AGN but also on larger, galactic and even intergalactic scales (Ciotti & Ostriker, 1997, 2001, 2007; Silk & Rees 1998; King 2003; Murray et al. 2005; Sazonov et al. 2005; Springel et al. 2005; Hopkins et al. 2005; Wang et al. 2006; Fabian et al. 2006; Thacker et al. 2006, and references therein).

In the first paper of this series (Proga 2007, Paper I hereafter), we reported on results from our first phase of gas dynamics studies in AGN on sub- and parsec-scales. This is a complex problem as it involves many aspects of physics such as multi-dimensional fluid dynamics, radiative and magnetic processes. Therefore, our approach was to set up simulations as simple as possible and to start with exploring the effects of the X-ray heating [important in the so-called preheated accretion, (e.g., Ostriker et al. 1976; Park & Ostriker 2001, 2007)] and radiation pressure on gas that is gravitationally captured by a black hole (BH). We adopted the numerical methods developed by Proga et al. (2000, PSK00 hereafter) for studying radiation driven disk winds in AGN. Generally, our simulations cover a relatively unexplored range of the distance from the central BH: we end where models of galaxies begin (e.g., Ciotti & Ostriker 2007; Springel et al. 2005) and we begin where models of BH accretion end (e.g., Hawley & Balbus 2002; Ohsuga 2007).

In Paper I, we presented results from axisymmetric time-dependent hydrodynamical (HD) calculations of gas flows. The flows were non-rotating and exposed to quasar radiation. We took into account X-ray heating and the radiation force due to electron scattering and spectral lines. To compute the radiation field, we considered an optically thick, geometrically thin, standard accretion disk as a source of UV photons and a spherical central object as a source of X-rays (a corona). The gas temperature, T and ionization state in the flow were calculated self-consistently from the photoionization and heating rate of the central object.

We found that, for a $10^8 M_{\odot}$ black hole with an accretion luminosity of 0.6 of the Eddington luminosity, the flow settles into a steady state and has two components: (1) an equatorial inflow and (2) a bipolar inflow/outflow with the outflow leaving the system along the disk rotational axis. The inflow is a realization of a Bondi-like accretion flow. The second component is an example of a non-radial accretion flow which becomes an outflow once it is pushed close to the rotational axis where the radiation pressure accelerate it outward. In some cases the outflow is heated by radiation so that it can be accelerated also by thermal expansion. Our main result was that the existence of the above two flow components is robust to the outer boundary conditions and the geometry and spectral energy distribution

of the radiation field. However, the flow properties are not robust. In particular, the outflow power and collimation is higher for the radiation dominated by the UV/disk emission than for the radiation dominated by the X-ray/central engine emission. Our most intriguing result was that a very narrow outflow driven by radiation pressure on lines can carry more energy and mass than a broad outflow driven by thermal expansion.

Here, we report on results from simulations that are basically reruns of those presented in Paper I, but with inclusion of gas rotation. Our goal is to assess how rotation changes the flow solution. In particular, we study how rotation changes the flow pattern, mass and energy fluxes, and temporal behavior. We also present results from a new set of simulations that illustrate how complex and dynamic the flow evolution can be even for relatively simple initial and boundary conditions. We describe our calculations in Section 2. We present our results in Section 3. The paper ends, in Section 4, with discussion and our conclusions.

2. Method

In this paper we extend the work presented in Paper I by relaxing some assumptions and simplifications. Our numerical HD calculations are in most respects as described by Paper I. Here we only describe the key elements of the calculations and list the changes we made. We refer a reader to Paper I and PSK00 for details.

We consider an axisymmetric HD flow accreting onto a supermassive BH. The flow is non-spherical because it is irradiated by an accretion disk. The disk radiation flux, $\mathcal{F}_{\text{disk}}$ is highest along the disk rotational axis and is gradually decreasing with increasing polar angle, θ : $\mathcal{F}_{\text{disk}} \propto |\cos \theta|$. The flow is also irradiated by a corona. We account for some effects of photoionization. In particular, we calculate the gas temperature assuming that the gas is optically thin to its own cooling radiation. We include the following radiative processes: Compton heating/cooling, X-ray photoionization heating, and recombination, bremsstrahlung and line cooling. We also take into account some effects of photoionization on radiation pressure due to lines (line force). Namely, we compute the line force using a value of the photoionization parameter, ξ and the analytical formulae due to Stevens & Kallman (1991). This procedure is computationally efficient and gives good estimates for the number and opacity distribution of spectral lines for a given ξ without detail information about the ionization state (see Stevens & Kallman 1991). Additionally, we take into account the attenuation of the X-ray radiation by computing the X-ray optical depth in the radial direction. To be consistent with our gas heating rates where we include X-ray photoionization but not UV photoionization, we do not account for attenuation of the UV radiation.

We assume that the total accretion luminosity, L has two components: $L_{\text{disk}} = f_{\text{disk}}L$ due to the accretion disk and $L_* = f_*L$ due to the corona. For simplicity, we assume that the disk emits only UV photons, whereas the corona emits only X-rays i.e., the system UV luminosity, $L_{\text{UV}} = f_{\text{UV}}L = L_{\text{disk}}$ and the system X-ray luminosity, $L_{\text{X}} = f_{\text{X}}L = L_*$ (in other words $f_{\text{UV}} = f_{\text{disk}}$ and $f_{\text{X}} = f_*$).

With the above simplifications, only the corona radiation is responsible for ionizing the flow to a very high ionization state. In our calculations, the corona contributes to the radiation force due to electron scattering but does not contribute to line driving. We note that metal lines in the soft X-ray band may have an appreciable contribution to the total radiation force in some cases. On the other hand, the disk radiation contributes to the radiation force due to both electron and line scattering.

We perform our calculations in spherical polar coordinates (r, θ, ϕ) assuming axial symmetry about the rotational axis of the accretion disk ($\theta = 0^\circ$).

Our computational domain is defined to occupy the angular range $0^\circ \leq \theta \leq 90^\circ$ and the radial range $r_{\text{i}} = 500 r_* \leq r \leq r_{\text{o}} = 2.5 \times 10^5 r_*$, where $r_* = 3r_{\text{S}}$ is the inner radius of the disk around a Schwarzschild BH with a mass, M_{BH} and radius $r_{\text{S}} = 2GM_{\text{BH}}/c^2$. The $r - \theta$ domain is discretized into zones. Our numerical resolution in the r direction consists of 140 zones. We fix the zone size ratio, $dr_{k+1}/dr_k = 1.04$ (i.e., the zone spacing is increasing outward). Gridding in this manner ensures good spatial resolution close to the inner boundary, r_{i} . In the θ direction, our numerical resolution consists of 50 zones. The zone size ratio is always $d\theta_l/d\theta_{l+1} = 1.0$ (i.e., grid points are equally spaced).

For the initial condition, in Paper I, we assumed spherical symmetry and set all HD variables to constant values everywhere in the computational domain. Here we will allow the gas to rotate.

2.1. Gas Rotation

In simulations with rotation, we break spherical symmetry of the initial and boundary conditions by introducing a small, latitude-dependent angular momentum. Namely, for large radii we assume the specific angular momentum, l , depends on the polar angle, θ , as

$$l(\theta) = l_0 f(\theta), \tag{1}$$

where $f = 1$ on the equator ($\theta = 90^\circ$) and monotonically decreases to zero at the poles (at $\theta = 0^\circ$ and 180°). The initial distribution of the rotational velocity is:

$$v_\phi(r, \theta) = \begin{cases} 0 & \text{for } r < 10^5 r_* \\ l/\sin \theta r & \text{for } r \geq 10^5 r_*. \end{cases} \quad (2)$$

We express the specific angular momentum on the equator as

$$l_0 = \sqrt{r'_c/6} c r_*, \quad (3)$$

where r'_c is the “circularization radius” on the equator in units of r_* for the Newtonian potential (i.e., $GM/r^2 = v_\phi^2/r$ at $r = r'_c r_*$). We adopt two forms for the function $f(\theta)$:

$$f_1(\theta) = \begin{cases} 0 & \text{for } \theta < \theta_o \text{ and } \theta > 180^\circ - \theta_o \\ l_0 & \text{for } \theta_o \leq \theta \leq 180^\circ - \theta_o, \end{cases} \quad (4)$$

and

$$f_2(\theta) = 1 - |\cos \theta|. \quad (5)$$

We also follow Paper I in setting the boundary conditions at the outer radius, r_o : to represent steady conditions at the outer radial boundary. During the evolution of each model, we apply the constraints that in the last zone in the radial direction, all HD quantities, except the radial velocity, are set to their initial values at all times. The radial velocity is allowed to float. In this paper we set $v_\phi(r_o, \theta)$ using eq. 2 whereas in Paper I, $v_\phi(r_o, \theta)$ was set to zero consistently with the initial conditions.

2.2. Mean Radiation Energy

One of the simplifications made in Paper I was an assumption that the radiation temperature, T_R [or more generally the spectral energy distribution (SED)] does not change with the position in the flow and it was set to the temperature of the isotropic corona radiation, T_X . This assumption finds justification in X-ray observations which show that quasar radiation heats a low-density gas nearly uniformly, on scales comparable to the Bondi radius, up to an equilibrium Compton temperature of about 2×10^7 K (Sazonov et al. 2005; Allen et al. 2006 and references therein). However, within our theoretical framework, the SED and T_R can change with position. For example, we assume that the UV/disk radiation decreases with increasing θ (see eq. 6 in Paper I). Thus even if the X-ray/central object radiation does not change with θ (see eq. 7 in Paper I) the ratio between the X-ray and UV fluxes increases with increasing θ . Consequently, our model predicts that radiation is softer near

the poles than near the equator. Moreover, we take into account the attenuation of the X-ray radiation but not of the UV radiation. Thus, for a given θ the ratio between the X-ray and UV fluxes can decrease if the X-ray optical depth is high. To test how important these effects are, we allow T_R to vary with position.

We introduce position-dependence of T_R in the following way. We start with the standard expression for the net Compton heating rate:

$$\mathcal{L} = n_e \frac{\sigma \mathcal{F}}{m_e c^2} (kT_R - 4kT), \quad (6)$$

where \mathcal{F} is the radiation flux, n_e is the electron number density (other symbols have their usual meaning).

As mentioned above, we consider two sources of radiation: a disk that emits UV photons with energy between 0 and 50 eV, and a corona that emits photons with energy above 50 eV. Each of these sources has its own mean photon energy, $\langle \epsilon \rangle$ or equivalently radiation temperature, ($\langle \epsilon \rangle = kT_R$). The radiation temperature of these two sources can be computed from:

$$kT_{\text{disk}} = \int_0^{50 \text{ eV}} h\nu \mathcal{F}_{\text{disk},\nu} d\nu / \int_0^{50 \text{ eV}} \mathcal{F}_{\text{disk},\nu} d\nu \quad (7)$$

and

$$kT_X = \int_{50 \text{ eV}}^{\infty} h\nu \mathcal{F}_{X,\nu} d\nu / \int_{50 \text{ eV}}^{\infty} \mathcal{F}_{X,\nu} d\nu. \quad (8)$$

We consider these temperatures as additional free parameters. We chose the radiation temperature of the disk to be 2×10^4 K and of the corona to be 2.9×10^8 K.

Having set the radiation temperature of the disk and corona radiation we can compute the radiation temperature of the total radiation field from:

$$T_R(\theta) = T_{\text{UV}} \frac{f_X R_T \exp(-\tau_X) + 2f_{\text{UV}} \cos \theta}{f_X \exp(-\tau_X) + 2f_{\text{UV}} \cos \theta}, \quad (9)$$

where $R_T = T_{X,\text{max}}/T_{\text{UV}}$. To obtain the expression above we used the definition of T_R and the formulae for the radiation fluxes from the disk and corona (eqs. 6 and 15 in Paper I). Practically, to account for the position-dependent radiation temperature, we adopt the same formulae for the radiative heating/cooling rates as in Paper I but replace T_X with T_R (see eqs. 19 and 20 in PSK). The seventh column in Table 1 shows the values of the adopted T_R or its range for cases when we use eq. 9.

We finish this section with a note about the gas temperature at the outer radius. This temperature is typically set to the Compton temperature assuming that the central X-rays heat a gas up to an equilibrium Compton temperature. However, in some of our simulations

the optical depth toward the radiation source or the local density in the flow is so high that radiation cannot heat a gas at large radii to the Compton temperature. In such cases, there is a mismatch between the gas temperature assumed at r_o (i.e., T_0) and that computed for r close to r_o .

It is possible that gas at large radii is heated not only by the central source but also by shocks or other sources such as supernovae. To mimic such sources of heating, we introduce an uniform background X-ray radiation, $\mathcal{F}_{X,b}$ in some of our simulations. We illustrate effects of this radiation by showing results of one model (run Crbgd), where we assumed $\mathcal{F}_{X,b} = 1.2 \times 10^7 \text{ erg cm}^{-2} \text{ s}^{-1}$, for which the gas with relatively low density is comptonized, e.g., for $\rho = 1 \times 10^{-20} \text{ g cm}^{-3}$, $\xi = 2.5 \times 10^4$ (we assume that T_R of the background radiation is the same as of the central source, that it $8 \times 10^7 \text{ K}$.)

3. Results

As in Paper I, we assume the mass of the nonrotating BH, $M_{\text{BH}} = 10^8 M_\odot$ and the disk inner radius, $r_* = 3 r_S = 8.8 \times 10^{13} \text{ cm}$ throughout this paper. We compute the total accretion luminosity as $L = \eta \dot{M}_a c^2 = 2\eta GM_{\text{BH}} \dot{M}_a / r_S$, where η and \dot{M}_a is the rest mass conversion efficiency and the mass accretion on BH, respectively. We assume a relatively high conversion efficiency appropriate for disk accretion onto a non-rotating BH, i.e., $\eta = 0.0833$.

We express the accretion luminosity in in units of the Eddington luminosity for the Schwarzschild BH, i.e., $L_{\text{Edd}} = 4\pi cGM_{\text{BH}}/\sigma_e$. We refer to this normalized luminosity as the Eddington number, $\Gamma \equiv L/L_{\text{Edd}} = (\sigma_e \dot{M}_a)/(8\pi cr_S)$.

Table 1 summarizes the properties of models from Paper I (runs A, B, B1, B2, B3, and C) and our new models (the other models listed in the table). Columns (2) to (11) give the input parameters that we varied: the Eddington number, Γ , the disk contribution to the total luminosity, f_{disk} , the corona contribution to the total luminosity, f_* , the UV contribution to the total luminosity, f_{UV} , the X-ray contribution to the total luminosity, f_X , the radiation temperature, T_R , the X-ray background radiation flux, $\mathcal{F}_{X,b}$, the gas temperature at the outer boundary, T_0 , the gas density at the outer boundary, ρ_0 , and the circularization radius, r'_c . Columns (12) to (17) give some of the gross properties of the solutions: the mass inflow rate through the outer boundary $\dot{M}_{\text{in}}(r_o)$, the net mass flux rate through the inner boundary $\dot{M}_{\text{net}}(r_i)$, the mass outflow rate through the outer boundary $\dot{M}_{\text{out}}(r_o)$, the maximum outflow velocity at the outer boundary, v_r , the outflow power carried out through the outer boundary in the form of kinetic energy, $P_k(r_o)$, and in the form of thermal energy, $P_{\text{th}}(r_o)$. Table 1 also explains our convention of labeling our runs. All other model parameters not listed in

Table 1 are as in Paper I.

3.1. Effects of Gas Rotation

Simulations without rotation presented in Paper I, show that an infalling gas collimates an outflowing gas and that the collimation increases with increasing radius. In addition, for a given Γ , the collimation increases with decreasing ratio between f_X and f_{UV} . Out of three cases explored in Paper I, case C with the smallest f_{UV}/f_X , shows the strongest collimation and the highest efficiency of turning an inflow into an outflow. Fig. 1 in Paper I and Fig. 1 here show that in run C the gas is siphoned off within a very narrow channel along the pole.

In Paper I, we argued that the collimation, outflow power and other results will likely change if one would allow for significant gas rotation. One would expect that the gas will converge toward the equator due to the combination of the centrifugal and gravitational forces. This, in turn, will likely broaden and weaken the outflow in the polar region because less gas will be pushed toward the polar region.

To test effects of rotation, we rerun models presented in Paper I with rotation. We set $r'_c = 300$ that is near the maximum value for which the flow will not circularize inside our computational domain. We do not consider higher r'_c at the moment because we want to avoid complexities that will result from formation a rotationally supported torus or disk inside the computational domain (e.g., Hawley, Smarr & Wilson 1984a; 1984b; Clarke, Karpik & Henriksen 1985; Hawley 1986; Molteni et al. 1994; Ryu et al. 1995; Chen et al. 1997; Toropin et al. 1999; Kryukov et al. 2000; Igumenshchev & Narayan 2002; Proga & Begelman 2003; Chakrabarti et al. 2004, and references therein). In these exploratory simulations, our choice of high r'_c , yielding low l , allows us then to study first, relatively simple flows and set a stage for modeling more complex flows with high l . We assume that the circularized gas will accrete onto SMBH on a viscous time scale. However, as we do not model this part of the flow, we do not consider any details of an actual process/es leading to transport of angular momentum. The transport is most likely due to magnetorotational instability (Balbus & Hawley 1991) but a contribution from the photon viscosity can be important in the case of high radiation luminosity.

We note that our choice of low l can be relevant to real QSOs because feeding a SMBH in QSO with gas of high l can be problematic. Namely, for high l , an accretion disk would form at large radii and be self-gravitating (e.g., Paczynski 1978; Shlosman & Begelman 1987). Converting disk material to stars could then starve the SMBH and QSO would be quenched (e.g., Goodman 2003). After reviewing variety of possibilities, Goodman (2003) suggested

that QSO disks do not extend beyond a thousand r_S so that they could be gravitationally stable. If so such the disks must be replenished with gas of small l as that we explore here.

Figure 1 presents the results for runs C, CR, and Cr. For run CR, a step function describes the angular distribution of angular momentum on the outer boundary (we set θ_0 to 45° in see eq. 4). For $45^\circ \leq \theta$, we assume that the specific angular momentum at the outer boundary equals l_0 , whereas for $\theta < 45^\circ$, $l = 0$. For run Cr, a smooth function describes l (see eq. 5). The figure shows the instantaneous density and temperature distributions, and the poloidal velocity field of the models. In addition, it shows the Compton radius corrected for the effects of radiation pressure due to electrons (see eq. [19] in Paper I) and the contours of the Mach number equal to one, ($M \equiv \sqrt{v_r^2 + v_\theta^2}/c_s = 1$, where $c_s = \gamma P/\rho$ is the sound speed).

The detailed calculations confirm our general expectations: compared with the non-rotating case, the outflow is less collimated and weaker in the rotating case. As Table 1 shows, in the runs with rotation (runs CR and Cr), the outflow power, $\dot{M}_{\text{out}}(r_o)$, and v_r are lower than those in the run without rotation (run C; compare also fig. 4 in Paper 1 with Figs. 2 and 3 here). Another difference is that in runs CR and Cr, gas does not cool as much as in run C, especially at small radii (i.e., $r' < 1 \times 10^5$). Comparison between runs C, CR, and Cr shows that in run CR the solution is an intermediate one between runs C and Cr which is not too surprising, given the step function is an intermediate distribution between zero- l and the one described by function f_1 . In particular, the outflow in run CR is less collimated than in run C and more collimated than in run Cr. One of new unexpected features that we found in run Cr is that the relatively cold outflow is fragmented and time-variable.

Although the flow in run Cr settles down into a time-averaged steady state, it is not as steady as in run C. An indication of this behavior can be found in Fig. 3 that shows three radial mass flow rates as a function of radius: the net rate, $\dot{M}_{\text{net}}(r)$, the inflow rate $\dot{M}_{\text{in}}(r)$, and the outflow rate $\dot{M}_{\text{out}}(r)$ (see eqs. 22, 23, 24 in Paper I for formal definitions). For a perfect steady state, one expects $\dot{M}_{\text{net}}(r) = \dot{M}_{\text{in}}(r) + \dot{M}_{\text{out}}(r) = \text{const}$ at all radii as in run C (see Fig. 4 in Paper I). However, in case Cr the above equation holds only at small radii, $r' \lesssim 10^4$ K. We note that contrary to \dot{M}_{out} , \dot{M}_{in} is a smooth function of radius. Thus the unsteadiness of in the flow appears to be caused by the unsteady behavior of the outflow, especially the outflow at large radii where it can cool down.

We relate the fragmentation and time-variability of the outflow to line force turning on abruptly when T decreases below $\sim 5 \times 10^4$ K and turning off when T increases again. Fig. 1 shows that T decreases in the regions where the inflow sharply turns into the outflow. The density there increases and the gas radiatively cools. The turning on of line force leads to an enhanced acceleration of the outflow, but this alone is not sufficient to fragment the outflow.

For example, in runs C and CR the cold outflow is not fragmented and is quite steady. Thus there must be another factor/s that may contribute to fragmentation and time-variability. We note that in run C, the outflow is nearly radial hence its inner parts shield the outer parts from the central radiation. Consequently, the outflow can not be heated downstream by the central radiation. However, in run Cr the outflow is not radial and the flow can be heated up downstream because, as its density decreases during acceleration, it is irradiated by stronger unattenuated X-ray flux. There the outflow orientation with respect to the radiation flux appears to be one of the key factors causing fragmentation and time-variability of the outflow. This conclusion is supported by the fact that even in run Cr, the outflow is not fragmented at large radii where the outflow becomes almost radial, and clumps merge with each other.

To show the variable solution in more details, in Fig. 4 we present a sequence of density maps of the inner part of the flow in run Cr at four different times. The left panel shows the flow at a time when a clump brakes from a high density filament at $z' \approx 1.5 \times 10^4 r_*$. Subsequent panels show how this and other clumps move outward and how they are stretched. Fig. 4 shows also formation a new clump (the second panel from the right). We find that clumps form usually at the same location (i.e., at $r' \approx 5 \times 10^3 r_*$ and $z' \approx 1.5 \times 10^4 r_*$) every 10^{11} s or so which is of order of a dynamical time scale at radius where the clumps form. Generally, despite the time-variability, the instantaneous maps shown in Fig. 1 are representative of run Cr because they show an example of a large scale inflow and outflow with continuous production of small scale clumps that merge at large radii (i.e., beyond $r' \gtrsim 10^5$).

Figs. 3 and 4 show that in runs CR and Cr the outflow power is dominated by the kinetic energy not the thermal energy. However, comparing with run C (see Fig. 4 in Paper I) the dominance is not as strong.

We conclude that in case C, rotation reduces the outflow collimation and the outward flux of mass and kinetic energy. Rotation also leads to fragmentation and time-variability of the outflow and an increase of the outward flux of the thermal energy. As expected, rotation does not change much the mass inflow rate through the outer boundary.

Figs. 5 and 6 show results for case B with and without rotation, i.e., runs B and Br (see also Fig. 3 in Paper I). In this case, rotational effects are almost the same as in case C. The main difference is that in run Br, an outflow does fragment and the overall flows settles down into a steady state. This however is understandable: in run Br, radiative heating is strong and the gas does not cool therefore line force does not turn on.

3.2. Effects of the position-dependent radiation temperature

We return now to case C and consider effects of the position-dependent T_R . Left panels of Fig. 7 and Fig. 8 show results for run Cx. In comparison with run C, the outflow in run Cx is broader. The mass outflow rate in run Cx is only slightly higher than in run C. However, the outflow rate almost cancels out the inflow rate so that the net rate is two orders of magnitude smaller than the mass flux through the outer boundary. Run Cx is a good example where AGN irradiation can significantly reduce the rate at which the central engine is fed with matter.

In run Cx, T_R is lower near the poles than near the equator. In addition, T_R near the pole is lower in run Cx than T_R in run C. The latter difference explains why the outflow in run Cx is so strong: the relatively low T_R in the polar region leads to a lower gas temperature in this region. This in turn leads to more mass being pushed towards the pole. This mass can then be effectively turned into an outflow because in the polar region the radiation flux is sub-Eddington and additionally, line-force turns on there because the gas temperature is low enough. In other words, the siphon effect seen in many of our simulations is very strong in run Cx.

Right panels of Fig. 7 and Fig. 9 show results for run Crx that is a rerun of run Cx with rotation. Comparing these two run, we find that effects of rotation in the simulations with the position-dependent T_R are similar to those in the simulations with constant T_X . Namely, rotation decreases the degree of the outflow collimation and decreases the outward flux of mass and kinetic energy. In addition, rotation leads to an increase of the outward flux of the thermal energy. In run Crx, the cold outflow is nearly radial and does not fragment as much as in run Cr.

In this paper, we do not present results for case A with rotation because in this case the flow is dominated by thermal effects and rotation does not change much the solution. However, we present here results for case A with the position-dependent T_R (run Ax) because they show new effects.

Fig. 10 compares results for runs A and Ax. In run Ax, the flow pattern is different that that seen in runs presented in Paper I or runs shown here so far. The dramatic difference is that in run Ax the equatorial inflow is replaced by an equatorial outflow. Generally, in run Ax there are equatorial and polar outflows both being fed by an inflow of gas at intermediate polar angles. The equatorial outflow is a simple consequence of the higher radiation temperature near the equator that leads to a high gas temperature and an enhanced thermal expansion. In the polar region, where the gas temperature is lower, an outflow is driven by thermal expansion assisted by radiation pressure on electrons.

Overall the flow pattern in run Ax is dominated by the outflow. This leads to the net mass inflow rate at small radii being one order of magnitude lower than the inflow rate at large radii.

We conclude that both rotation and position-dependent T_R lead to qualitative and quantitative changes in the flow. Most prominent of them are weaker collimation and fragmentation of the outflow in cases with rotations, and production of an thermal equatorial outflow in cases with position-dependent T_R .

3.3. Complex Case

A realistic model of accretion flows should include many physical effects. Here, we focused on the role of gas rotation and position-dependent T_R . We consider our simulations just as exploratory tests. These tests support the notion that AGN radiation can play a very important role in determining the ionization structure and dynamics of matter on sub- and parsec-scales. We finish the presentation of our models with showing results for two runs that illustrate how complex the flow dynamics can be even in a very simple set-up as the one we focus on here.

One of our motivations is to understand gas dynamics in broad line regions (BLRs) and Narrow Line Regions (NRL) so characteristic to AGN. These regions are thought to be made of cold gas clouds moving randomly or nearly randomly and having a small filling factor (e.g., Krolik 1999 and reference therein). Formation, evolution and other key aspects of these clouds are not well understood. Our simulations show that an accretion flow which is initially smooth and spherical can break into inflows and outflows. In cases with rotation, we have seen outflows fragmented due to line force and X-ray irradiation. These results raise the following question: can we produce many cold clouds with a small filling factor. The answer seems to be yes as we show in Figs. 12 and 13, and 14.

Figs. 12, 13, and 14 compare results for case C with $\Gamma = 0.9$ and $\rho_o = 10^{-20}$ g cm⁻³. Left panels in Fig. 12 show results for run Crgd. The density and temperature distribution and as well as some other properties of this run differ a lot from other runs shown here. The main difference is a much larger dynamical range in the temperature and density plus the fact that the flow is far from reaching any steady state. However, close inspection of the results from run Crgd show that the flow pattern is similar to that seen in most other runs: there is an equatorial inflow and a bipolar outflow. The latter is not fragmented because it is radial in agreement with our explanation of the outflow fragmentation. The large dynamical range in the density and temperature in run Crgd is a simple consequence of the higher

density at the outer boundary. A high density gas can cool much faster than a low density gas. In this run the gas is also heated by shocks because for $\Gamma = 0.9$ radiation pressure of electrons alone can drive a powerful and broad outflow that collides with an inflowing gas.

As we discussed in §2.2, an accretion flow at large radii does not have to be heated by the central radiation source. The lower left panel in Fig. 12 illustrates this point as one can see that near the equator a good fraction of the inflow is relatively cold. One of the predictions of such a model is that for a wide range of the inclination angle, this cold gas should produce absorption lines redshifted with respect to the systematic velocity. However, such lines are not being observed.

The problem of large scale accretion of cold gas can be easily overcome by introduction of non-central source of heating. Right panels in Fig. 12, show results for run Crbgd which is a rerun of model Crgd with the X-ray background radiation (see §2.2).

In run Crbgd, there are no large regions of shock heated gas. The only region where shock heating is important is in a narrow polar region of a low density. The background radiation heating in this run keeps the gas from rapid cooling which in turn can lead to abrupt turn-on of line driving and strong expulsion of gas as seen in run Crgd.

Comparing runs Cr and Crbgd, we see that an outflow tends to fragment more if the gas density is higher. The density and temperature maps show that the outflow occupies a relatively large fraction of the computational domain. However, Fig. 14 shows that this outflow does not change much the overall mass budget. As in run Cr, this is caused by rotation that reduces the amount of gas that is pushed toward the polar region where it can be siphoned off.

4. Conclusions

We have calculated a series of models for rotating flows that are under the influence of supermassive BH gravity and radiation from an accretion disk surrounding the BH. We seek to determine self-consistently what fraction of the flow is gravitationally captured by the BH or what fraction is driven away by thermal expansion and radiation pressure. This work is an extension of the work presented in Paper I, where nonrotating flows were studied. Here, we consider effects of rotation and of a position-dependent radiation temperature, density at large radii, and an uniform X-ray background radiation.

As in the non-rotating case, the rotating flow settles into a configuration with two components (1) an equatorial inflow and (2) a bipolar inflow/outflow with the outflow leaving

the system along the pole. However, the rotating flow does not reach a steady state. In addition, rotation reduces the outflow collimation and the outward flux of mass and kinetic energy. Moreover rotation increases the outward flux of the thermal energy and can lead to fragmentation and time-variability of the outflow. In future, we plan to check whether thermal instability can contribute to fragmentation and time-variability of the outflow. As expected, rotation does not change much the mass inflow rate through the outer boundary.

In our model, the radiation comes from an UV emitting disk and X-ray emitting spherical corona. As a result, the radiation temperature is position-dependent: in the polar region radiation is dominated by a softer disk component whereas near the equator, radiation is dominated by a harder corona component. The two main changes due this position-dependence are: (i) an increase in the power of the outflow in the polar region and (ii) development of a large scale thermally driven outflow in the equatorial region.

Overall, we conclude that our exploratory study provides an additional support to the idea that AGN radiation can significantly change gas dynamics and photoionization structure on sub-parsec- and parsec-scales. As it have been discussed and shown in the past, we found that AGN radiation can significantly reduce the rate at which the central BH is fed with matter (e.g., Figs. 8 and 13). This result should not depend on the inner radius of the computational domain because most of the outflow is launched from a radius larger than the inner radius of the computational domain. However, we note when reducing the inner radius of the computational domain one should also consider additional processes, in particular, disk accretion and disk winds and jets. Thus our mass inflow rate should be viewed only as an upper limit for the BH accretion rate.

Our results emphasize also a little appreciated feature, i.e., AGN radiation can drive a non-spherical, multi-temperature and very dynamic flow pattern. This result may have implications for the problem of AGN feedback and the problem of the origin, geometry and physics of NLR and BLR.

This work is supported by NASA through grants HST-AR-10680 and HST-AR-11276 from the Space Telescope Science Institute, which is operated by the Association of Universities for Research in Astronomy, Inc., under NASA contract NAS5-26555.

REFERENCES

- Allen, S.W., Dunn, R.J.H., Fabian, A.C., Taylor, G.B., Reynolds, C.S. 2006, MNRAS, 372, 21

- Ciotti L., Ostriker J. P., 1997, *ApJ*, 487, L105
- Ciotti L., Ostriker J. P., 2001, *ApJ*, 551, 131
- Ciotti L., Ostriker J. P., 2007, *ApJ*, 665, 1038
- Clarke, D., Karpik, S., & Henriksen, R.N. 1985, *ApJS*, 58, 81
- Chakrabarti, S. K., Acharyya, K., & Molteni, D. 2004, *A&A*, 421, 1
- Chen, X., Taam, R.E., Abramowicz, M.A., & Igumenshchev, I.V. 1997, *MNRAS*, 285, 439
- Goodman, J. 2003, *MNRAS*, 339, 937
- Fabian, A. C., Celotti, A., & Erlund, M. C. 2006, *MNRAS*, 373, L16
- Hawley, J.F., Smarr, L.L., & Wilson, J.R. 1984a, *ApJ*, 277, 296
- Hawley, J.F., Smarr, L.L., & Wilson, J.R. 1984b, *ApJS*, 55, 211
- Hawley, J. F., & Balbus, S. A. 2002, *ApJ*, 573, 738
- Hopkins, P.F., Hernquist, L., Cox, T.J., Di Matteo, T., Martini, P., Robertson, B., & Springel, V. 2005, *ApJ*, 630, 705
- Igumenshchev, I.V. & Narayan, R. 2002, *ApJ*, 566, 137
- King A., 2003, *ApJ*, 596, L27
- Krolik, J.H. 1999, *Active galactic nuclei: from the central black hole to the galactic environment*, Princeton, N.J.: Princeton University Press
- Kryukov, I.A., Pogorelov, N.V., Bisnovatyi-Kogan, G.S., Anzer, U., & Börner, G. 2000, *A&A*, 364, 901
- Molteni, D., Lanzafame, G., & Chakrabarti, S. 1994, *ApJ*, 425, 161
- Murray N., Quataert E., Thompson T. A., 2005, *ApJ*, 618, 569
- Ostriker, J.P., Weaver, R., Yahil, A., & McCray, R. 1976 *ApJ*, 208, 610
- Ohsuga, K. 2007, *ApJ*, 659, 2050
- Paczynski, B., 1978, *Acta Astron.*, 28, 91
- Park, M.-G., & Ostriker, J. P. 2007, *ApJ*, 549, 100

- Park, M.-G., & Ostriker, J. P. 2007, ApJ, 655, 88
- Proga, D. 2007, ApJ, 661, 693 (Paper I)
- Proga, D., & Begelman, M. C. 2003, 582, 69
- Proga, D., Stone, J.M., & Kallman, T.R. 2000, ApJ, 543, 686 (PSK00)
- Ryu, D., Brown, G.L, Ostriker, J.P., & Loeb, A. 1995, ApJ, 452, 364
- Sazonov, S. Y., Ostriker, J. P., Ciotti, L., & Sunyaev R. A. 2005, MNRAS, 358, 168
- Shlosman I., & Begelman M.C., 1987, Nat, 329, 810
- Silk, J. & Rees, M. J. 1998, A&A, 331, L1
- Springel V., Di Matteo T., & Hernquist L. 2005, ApJ, 620, L79
- Stevens, I. R., & Kallman, T. R. 1990, ApJ, 365, 321
- Thacker, R. J., Scannapieco, E., & Couchman, H. M. P. 2006, ApJ, 653, 86
- Toropin, Y.M., Toropina, O.D., Savelyev, V.V., Romanova, M.M., Chechetkin, V.M., & Lovelace, R.V.E. 1999, ApJ, 517, 906
- Wang, J.-M., Chen, Y.-M.; Hu, C. 2006, ApJ, 637, L85

Table 1: Summary of results

Run	Γ	f_{disk}	f_*	f_{UV}	f_{X}	T_{R} (1)	$\mathcal{F}_{\text{X,b}}$ (2)	T_0 (1)	ρ_0 (3)	r'_c (4)	$\dot{M}_{\text{in}}(r_o)$ (5)	$\dot{M}_{\text{net}}(r_i)$ (5)	$\dot{M}_{\text{out}}(r_o)$ (5)	v_r (6)	$F_{\text{k}}(r_o)$ (7)	$P_{\text{th}}(r_o)$ (7)
A	0.6	0.5	0.5	0.5	0.5	4	0	1	1	0	-4	-1	3	700	2	4
Ax	0.6	0.5	0.5	0.5	0.5	4.8-14.5	0	1	1	0	-0.8	-0.1	0.7	400	0.1	2
B	0.6	0.8	0.2	0.8	0.2	4	0	1	1	0	-8	-3	5	4000	100	0.8
Br	0.6	0.8	0.2	0.8	0.2	4	0	1	1	300	-8	-5	3	1300	4	0.5
B1	0.6	0.8	0.2	0.8	0.2	4	0	1/10	1	0	-0.5	-0.09	0.41	1500	0.5	0.8
B2	0.6	0.8	0.2	0.8	0.2	4	0	1/3	1	0	-2	-0.4	1.6	1700	2	2
B3	0.6	0.8	0.2	0.8	0.2	4	0	3	1	0	-9	-5	4	400	3	0.8
C	0.6	0.95	0.05	0.95	0.05	4	0	1	1	0	-9	-1	8	6700	700	0.03
CR	0.6	0.95	0.05	0.95	0.05	4	0	1	1	300	-10	-8	3	600	3	0.2
Cr	0.6	0.95	0.05	0.95	0.05	4	0	1	1	300	-10	-4	6	1000	10	0.2
Cx	0.6	0.95	0.05	0.95	0.05	0.3-14.5	0	1	1	0	-11	-0.15	10.85	7000	300	0.03
Crx	0.6	0.95	0.05	0.95	0.05	0.3-14.5	0	1	1	300	-11	-2	3	500	10	0.01
Crgd	0.9	0.95	0.05	0.95	0.05	4	0	10	10	300	-115	-5	110	2500	1000	10.
Crbgd	0.9	0.95	0.05	0.95	0.05	4	1.2	10	10	300	-150	-120	30	3700	30	5.

Note. — (1) in 2×10^7 K, (2) in 10^7 erg cm $^{-2}$ s $^{-1}$, (3) in 10^{-21} g cm $^{-3}$, (4) in r_* , (5) in 10^{25} g s $^{-1}$, (6) in km s $^{-1}$, (7) in 10^{40} erg s $^{-1}$. We use the following convention to label our runs: the first character refers to the values of f_{X} and f_{UV} : A is for $f_{\text{UV}} = 0.5$ and $f_{\text{X}} = 0.5$, B is for $f_{\text{UV}} = 0.8$ and $f_{\text{X}} = 0.2$, and C is for $f_{\text{UV}} = 0.95$ and $f_{\text{X}} = 0.05$. Runs A, B, and C, are the fiducial runs. If the first character is followed by a lower case letter or letters or a number, it means that it is the same run, but modified by introduction of: rotation (letter 'R' and 'r' if we use eq. 4 or 5, respectively), the position-dependent T_{R} (letter 'x'), the X-ray background radiation (letter 'b'), a higher Γ (letter 'g'), and a higher ρ_0 (letter 'd'). The numbers 1, 2, and 3 correspond respectively to $T_{\text{R}} = 1/10, 1/3, 3$ in units of 2×10^7 K.

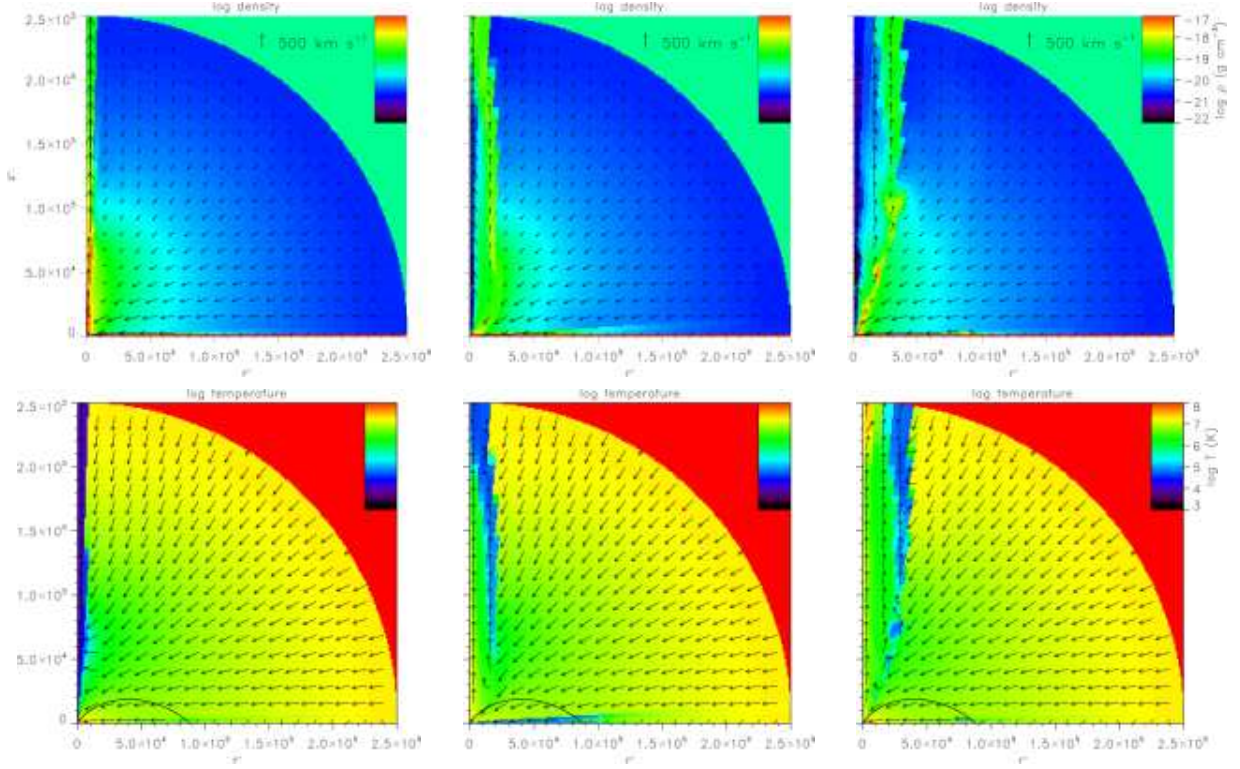


Fig. 1.— Comparison of the results for runs C, CR, and Cr (left, middle, and right column, respectively) *Top row*: Maps of logarithmic density overplotted by the poloidal velocity. For clarity, the arrows are plotted with the maximum velocity set to 1000 km s^{-1} . The solid curves show are the contours of the Mach number equal one. *Bottom row*: Maps of logarithmic temperature overplotted by the direction of the poloidal velocity. The solid curve in the bottom left corner marks the position of the Compton radius corrected for the effects of radiation pressure due to electron scattering (see eq. 19 in Paper I). The length scale is in units of the inner disk radius (i.e., $r' = r/r_*$ and $z' = z/r_*$).

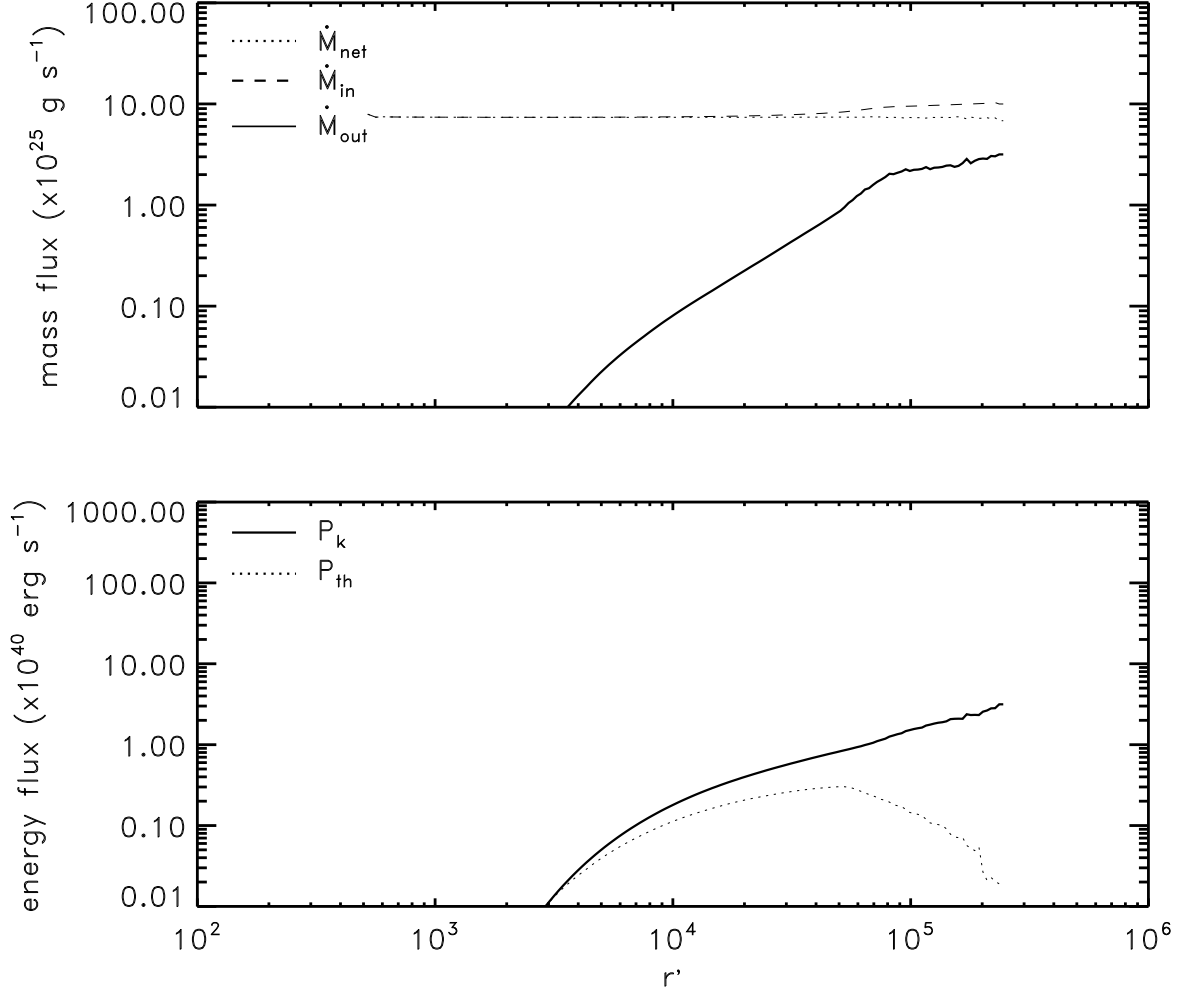


Fig. 2.— *Top panel:* The mass flux rates as a function of radius for run CR. The solid, dashed, and dotted line corresponds to the outflow, inflow, and net rates, respectively (see eqs. 20, 21, and 22 in Paper 1 for the formal definitions). Note that the absolute value of the inflow and net rates are plotted because these quantities are negative. *Bottom panel:* The energy fluxes carried out by the outflow as a function of radius in run CR. The solid and dashed line corresponds to the kinetic and thermal energy flux, respectively (see eqs. 23 and 24 for the formal definitions). The length scale is in units of the inner disk radius (i.e., $r' = r/r_*$).

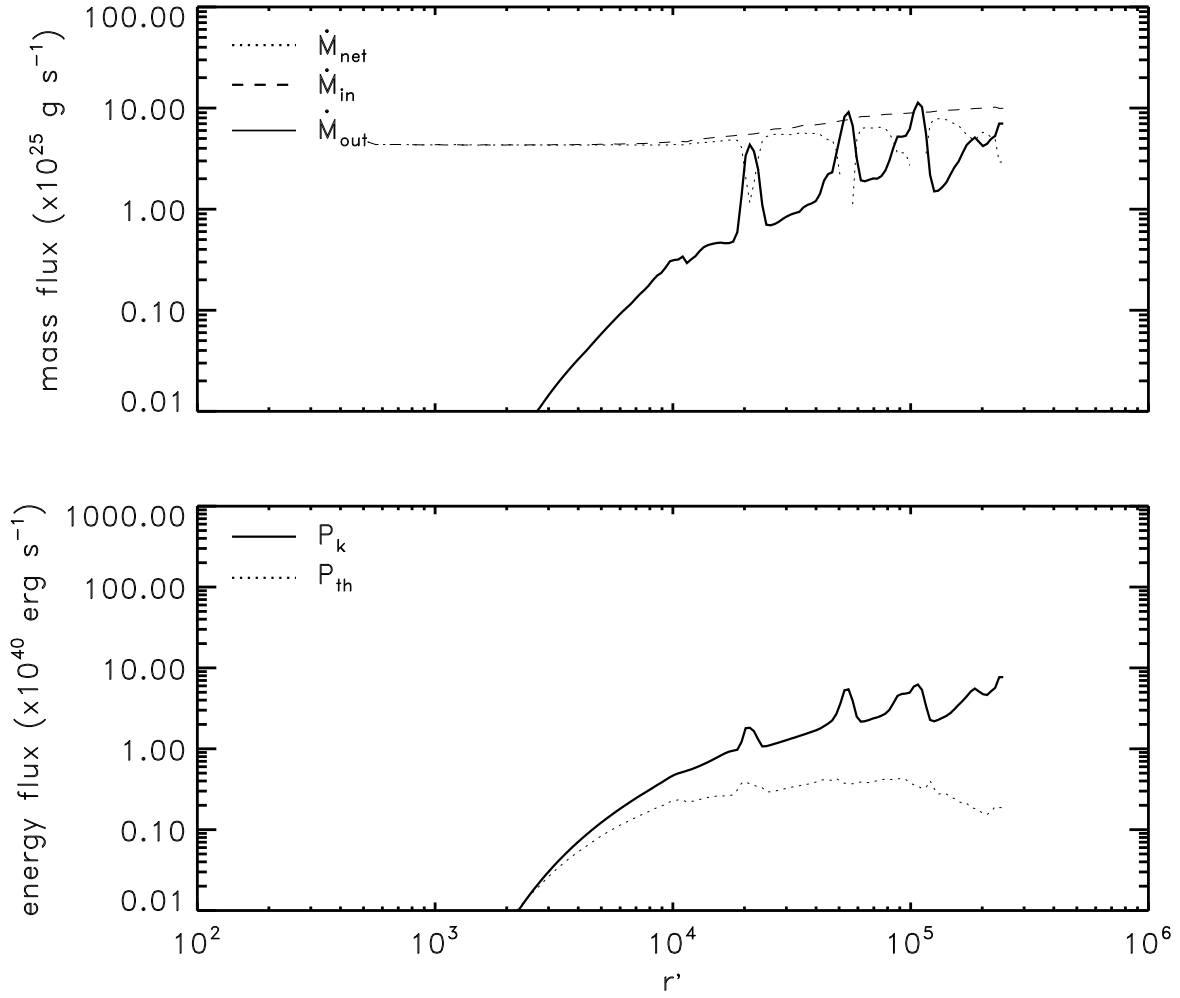


Fig. 3.— As in Fig. 2, but for run Cr.

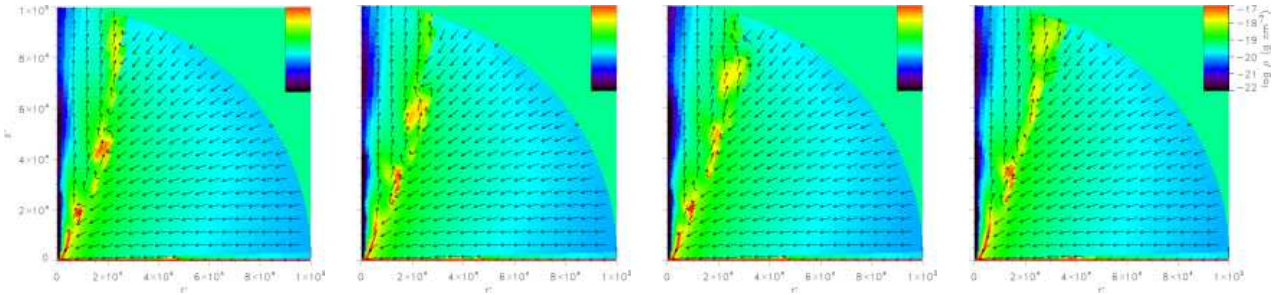


Fig. 4.— A sequence of density maps for the inner part of run CR after $4.95, 5.00, 5.05,$ and 5.10×10^{12} s (from left to right). Run CR is an example of unsteady flow discussed in detail in section 3.1. As in fig. 1, the length scale is in units of the inner disk radius (i.e., $r' = r/r_*$ and $z' = z/r_*$). However, the r' and z' ranges are 2.5 time smaller compared to fig. 1.

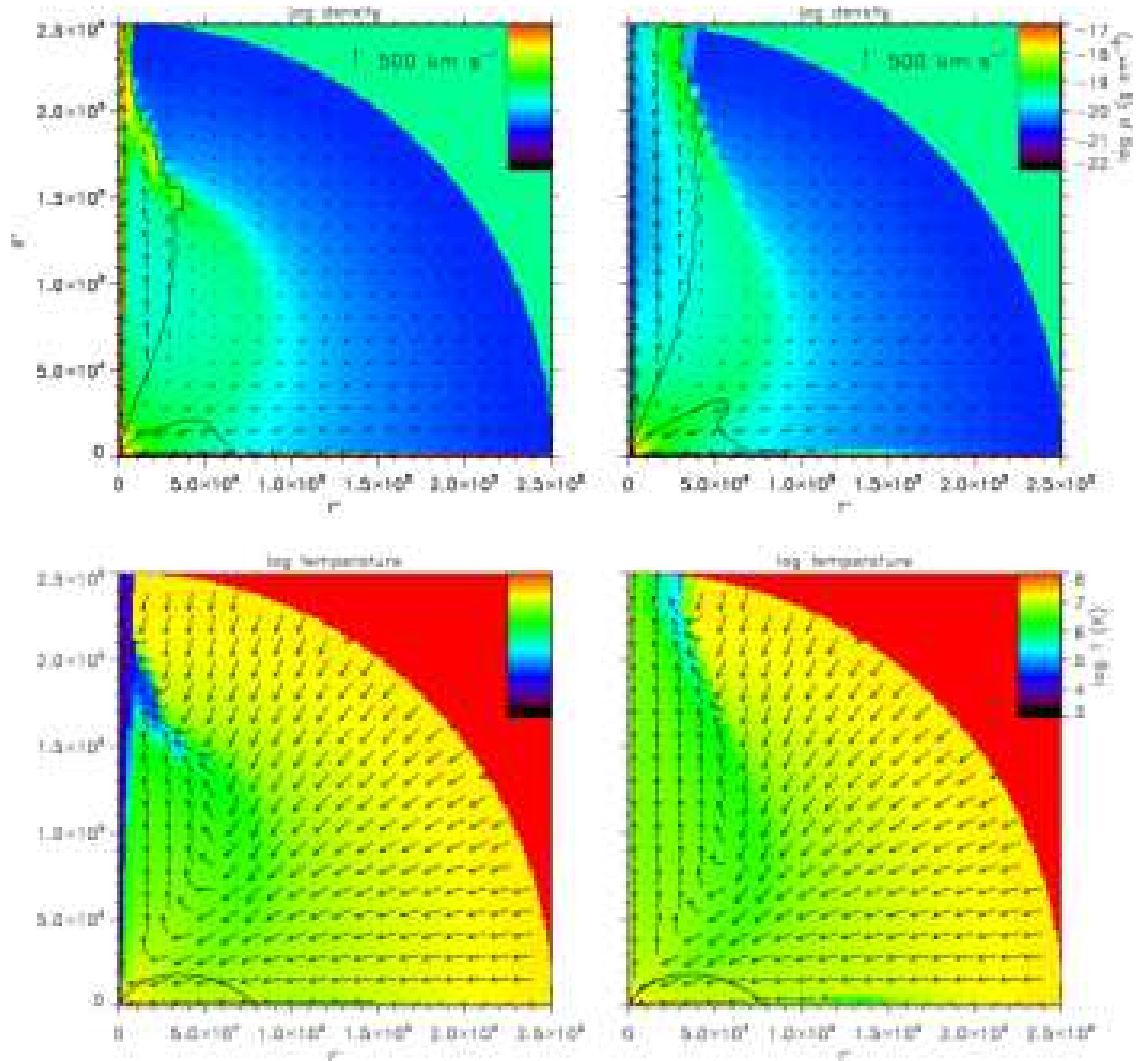


Fig. 5.— As in Fig. 1, but for runs B and Br.

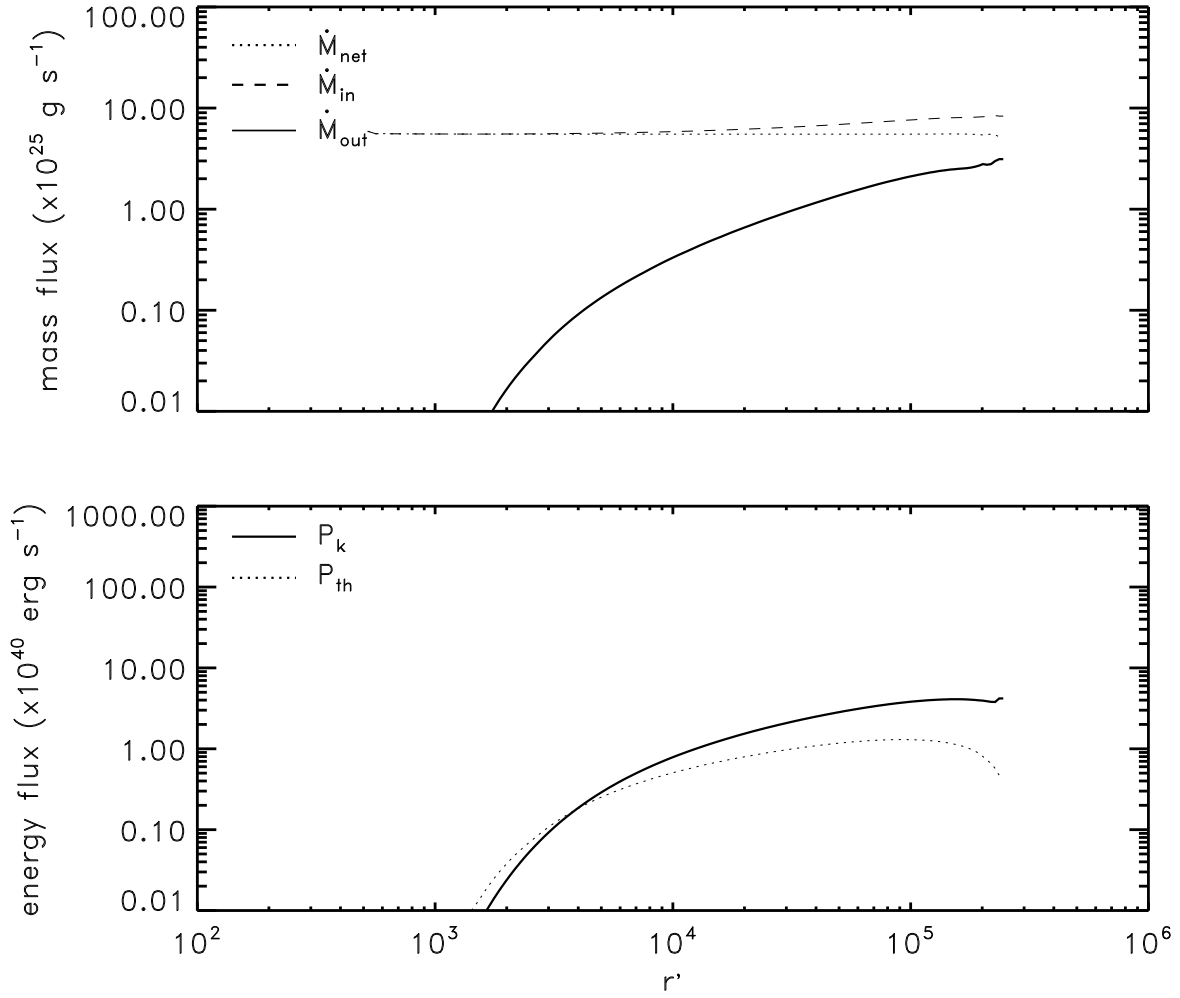


Fig. 6.— As in Fig. 2, but for run Br.

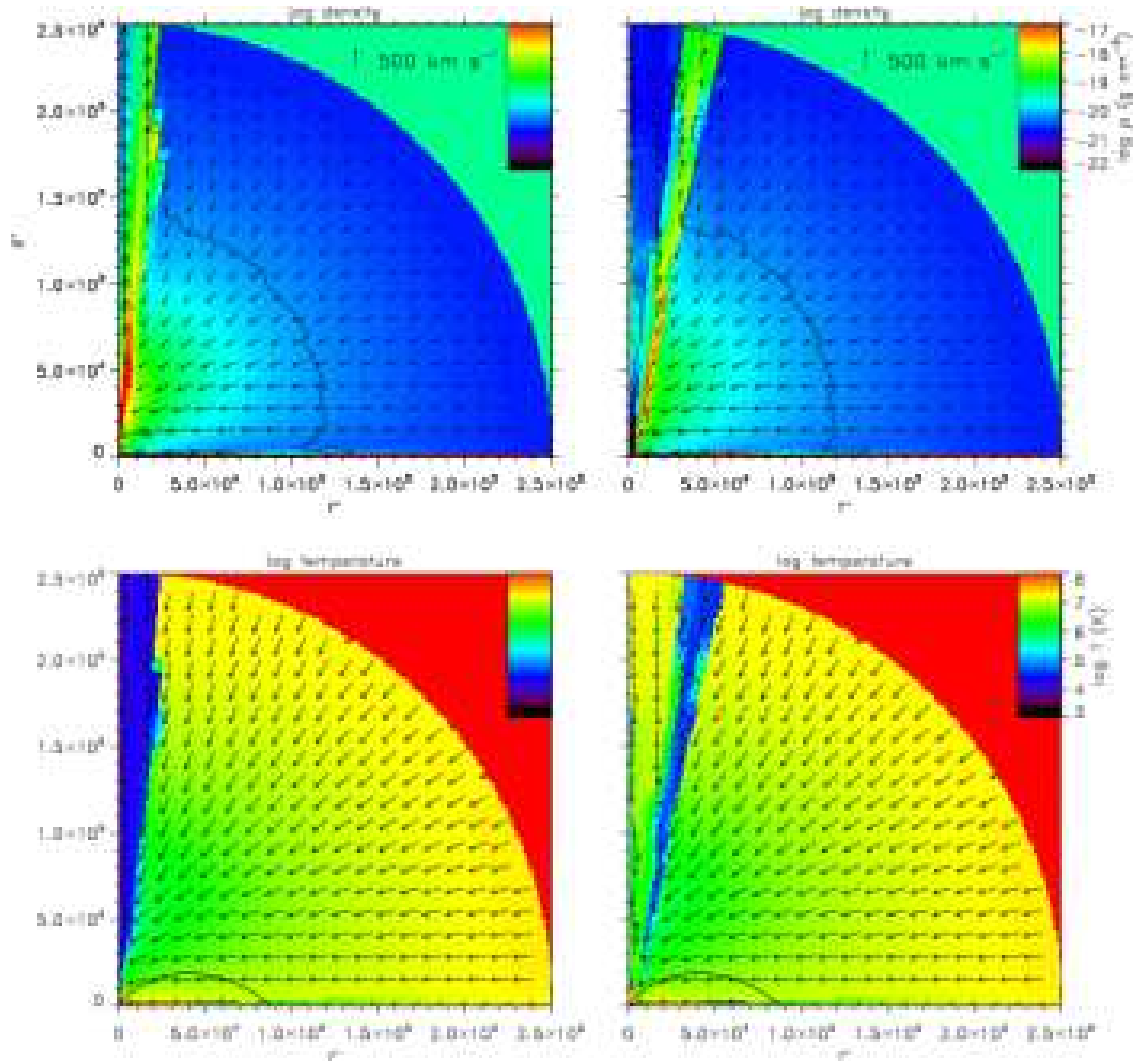


Fig. 7.— As in Fig. 1, but for runs Cx and Crx.

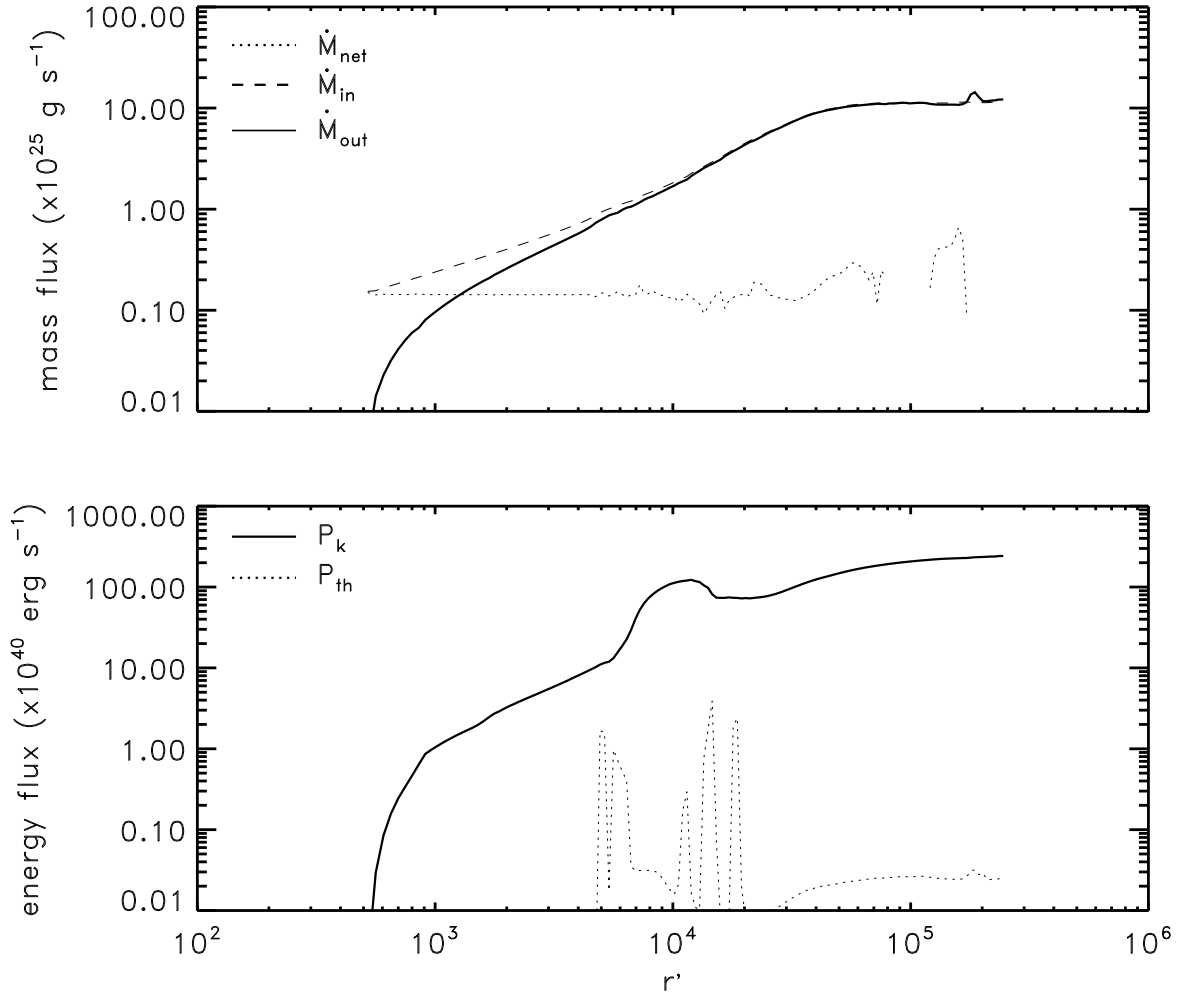


Fig. 8.— As in Fig. 2, but for run Cx.

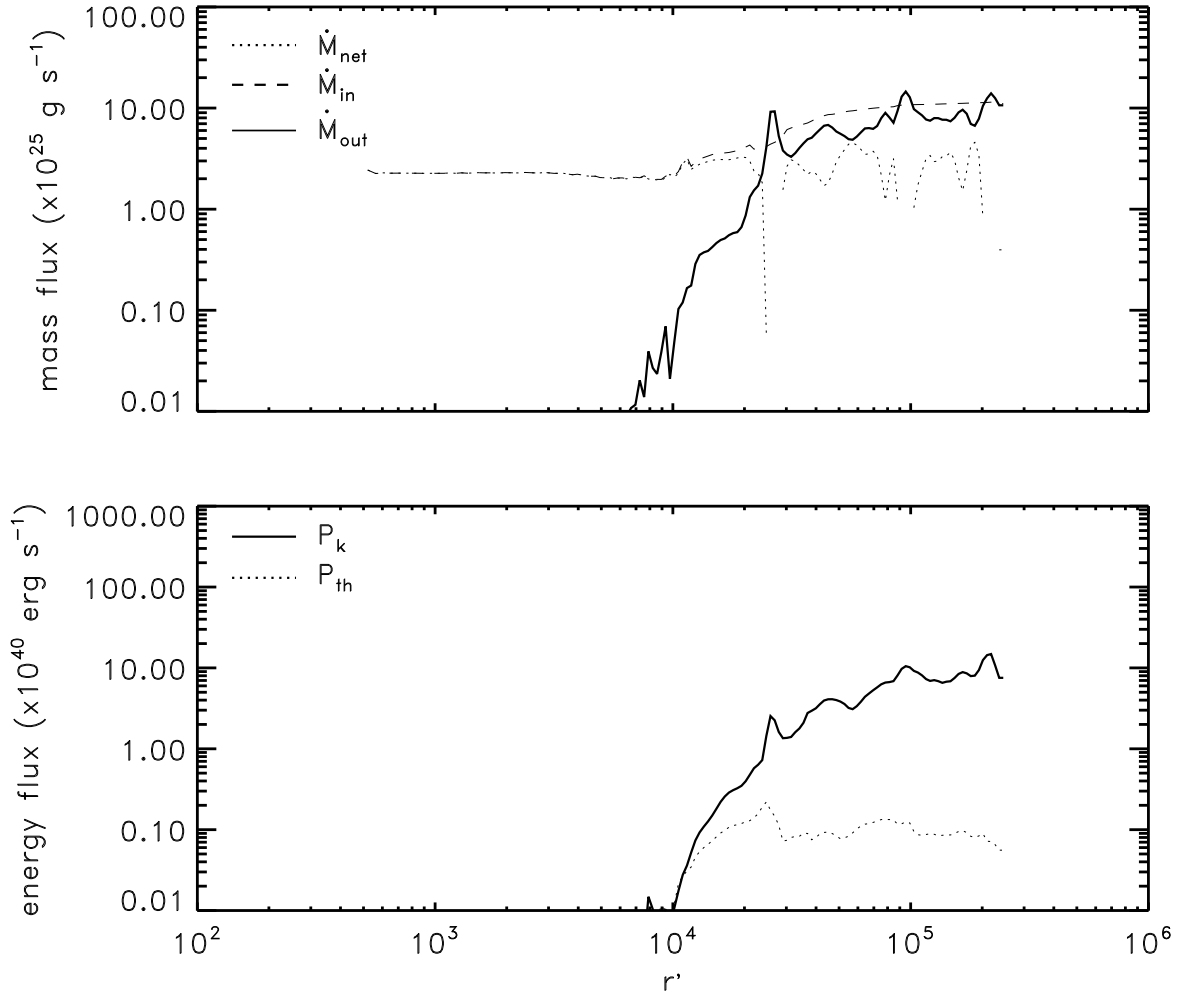


Fig. 9.— As in Fig. 2, but for run Crx.

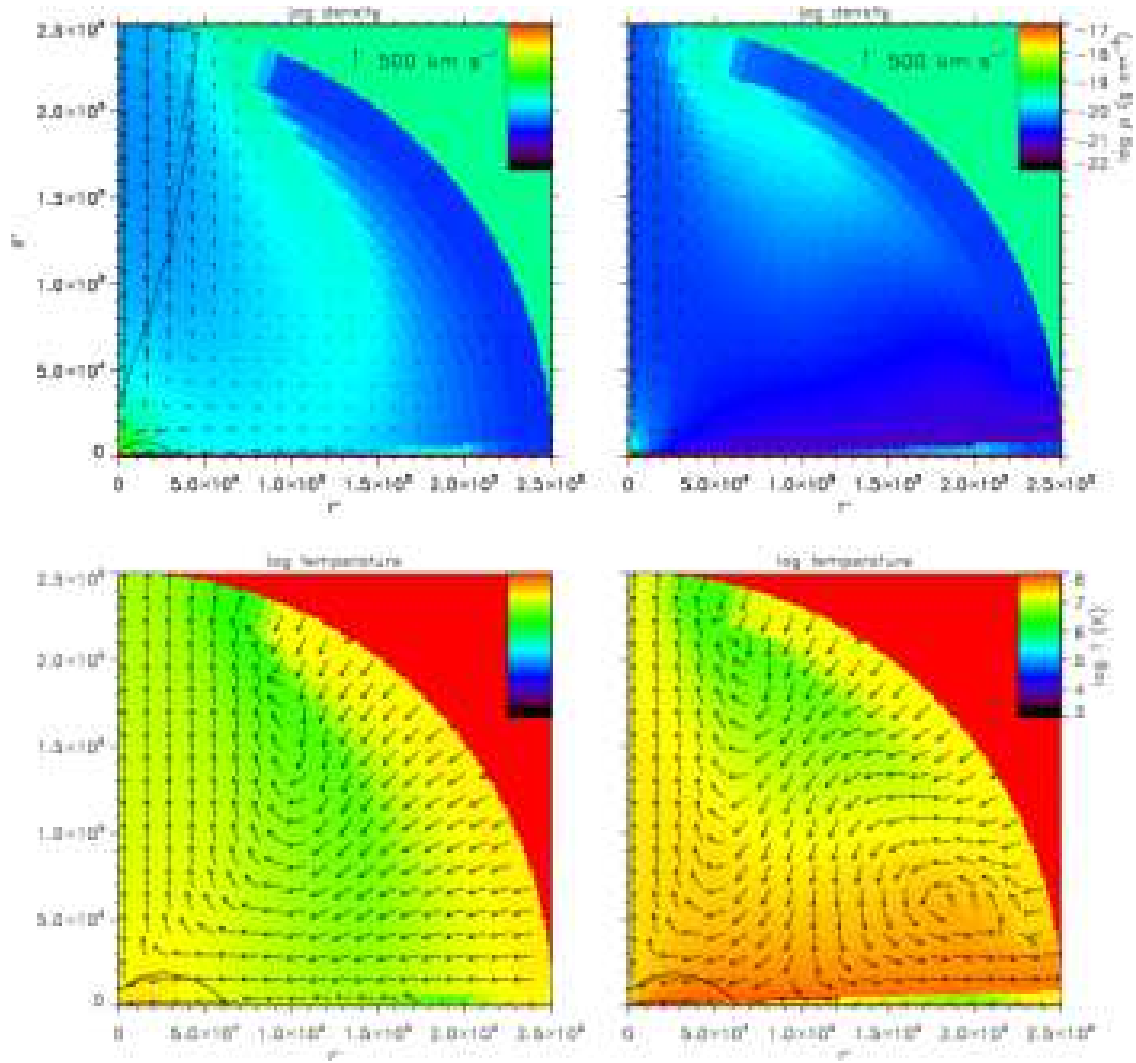


Fig. 10.— As in Fig. 1, but for runs A and Ax.

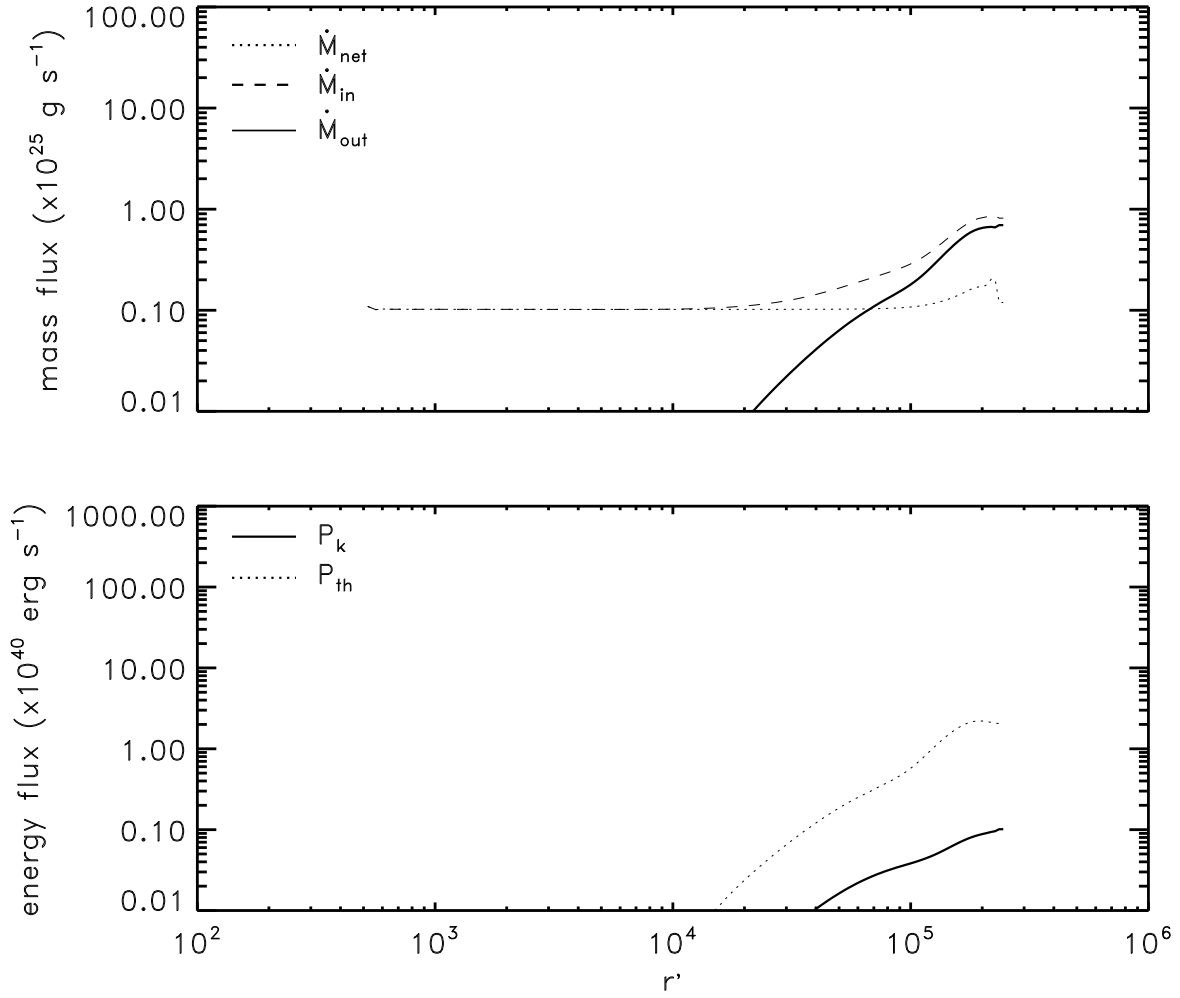


Fig. 11.— As in Fig. 2, but for run Ax.

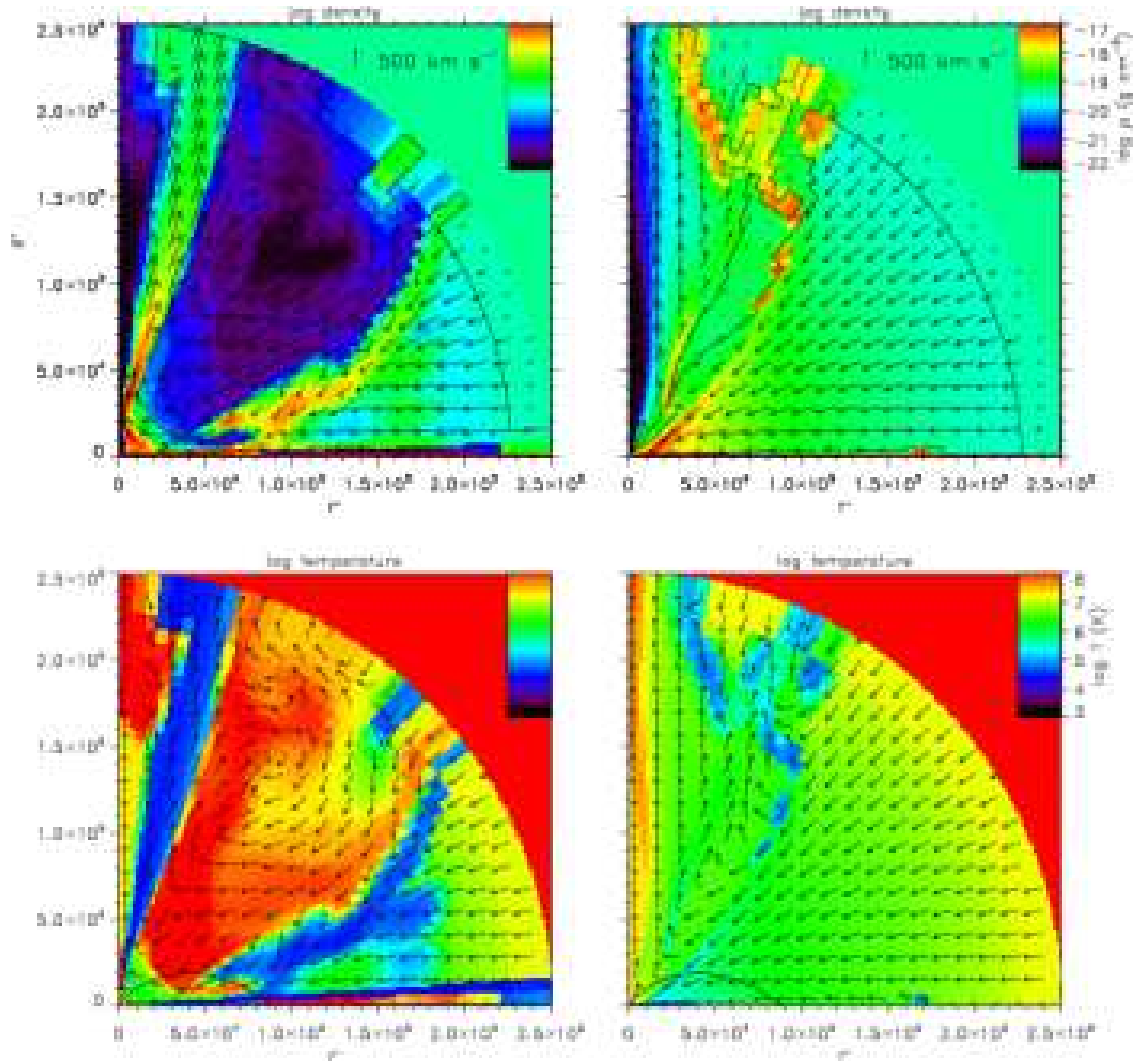


Fig. 12.— As in Fig. 1, but for runs Crgd and Crbgd.

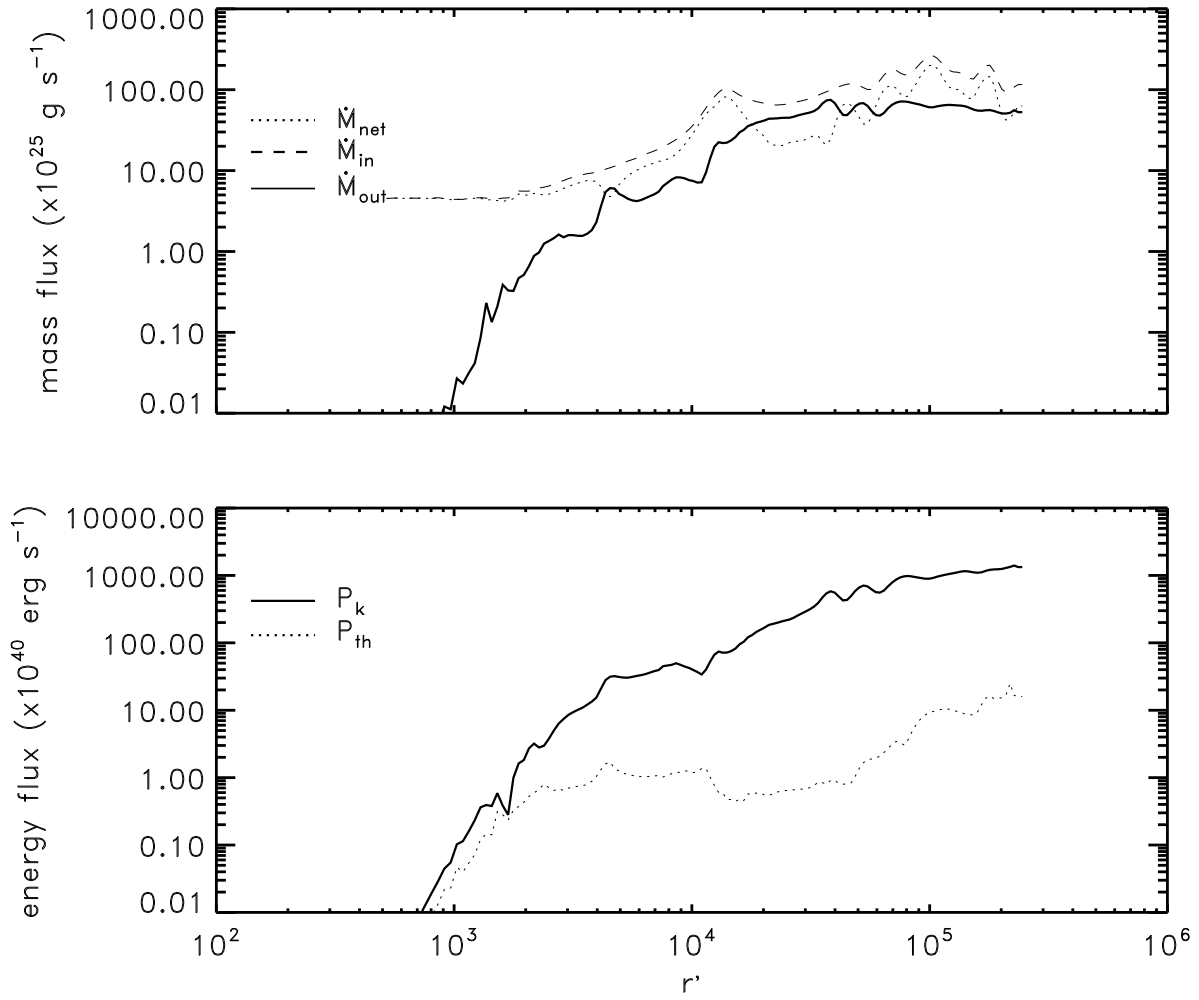


Fig. 13.— As in Fig. 2, but for run Crgd. Note an increase range along the y-axis compared to Fig 2.

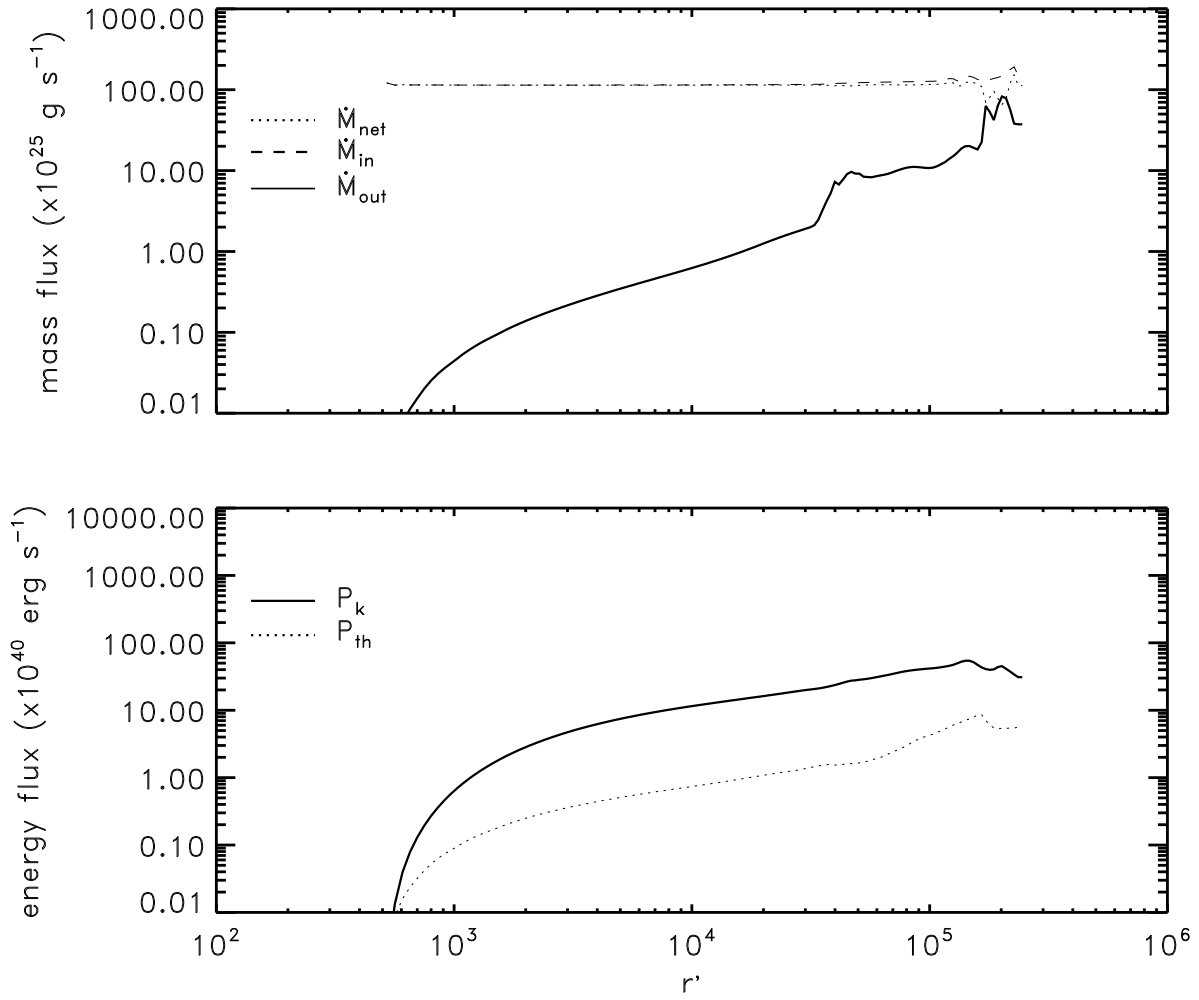


Fig. 14.— As in Fig. 2, but for run Crbgd. Note an increase range along the y-axis compared to Fig 2.